Since January 2020 Elsevier has created a COVID-19 resource centre with free information in English and Mandarin on the novel coronavirus COVID-19. The COVID-19 resource centre is hosted on Elsevier Connect, the company's public news and information website.

Chemical Engineering Journal 466 (2023) 143330

Contents lists available at ScienceDirect

Chemical Engineering Journal

journal homepage: www.elsevier.com/locate/cej

Multi-bioinspired hierarchical integrated hydrogel for passive fog harvesting and solar-driven seawater desalination

Yi Zhang [a], Feifei Wang [a], Yongtao Yu [a], Jiajia Wu [a], Yingying Cai [a], Jian Shi [c,*], Hideaki Morikawa [b,c,*], Chunhong Zhu [b,c,*]

[a] Graduate School of Medicine, Science and Technology, Shinshu University, 3-15-1 Tokida, Ueda, Nagano 386-8567, Japan
[b] Institute for Fiber Engineering (IFES), Interdisciplinary Cluster for Cutting Edge Research (ICCER), Shinshu University, 3-15-1 Tokida, Ueda, Nagano 386-8567, Japan
[c] Faculty of Textile Science and Technology, Shinshu University, 3-15-1 Tokida, Ueda, Nagano 386-8567, Japan

ARTICLE INFO

Keywords:
Bioinspiration
Water harvesting
Solar evaporation
Desalination
Hierarchical structure

ABSTRACT

In recent years, with the outbreak and epidemic of the novel coronavirus in the world, how to obtain clean water from the limited resources has become an urgent issue of concern to all mankind. Atmospheric water harvesting technology and solar-driven interfacial evaporation technology have shown great potential in seeking clean and sustainable water resources. Here, inspired by a variety of organisms in nature, a multi-functional hydrogel matrix composed of polyvinyl alcohol (PVA), sodium alginate (SA) cross-linked by borax as well as doped with zeolitic imidazolate framework material 67 (ZIF-67) and graphene owning macro/micro/nano hierarchical structure has successfully fabricated for producing clean water. The hydrogel not only can reach the average water harvesting ratio up to 22.44 g g^{-1} under the condition of fog flow after 5 h, but also be capable of desorbing the harvested water with water release efficiency of 1.67 kg m^{-2} h^{-1} under 1 sun. In addition to excellent performance in passive fog harvesting, the evaporation rate over 1.89 kg m^{-2} h^{-1} is attained under 1 sun on natural seawater during long-term. This hydrogel indicates its potential in producing clean water resources in multiple scenarios in different dry or wet states, and which holds great promise for flexible electronic materials and sustainable sewage or wastewater treatment applications.

1. Introduction

Owing to the impact of population growth, economic development, and the outbreak of the COVID-19 epidemic in recent years, a large amount of clean water resources is being consumed, the water crisis is getting worse year by year [1,2]. Water scarcity is a huge challenge for the world as the demand for clean water continues to increase [3]. Two-thirds of the world's population lives under severe water shortage conditions for at least one month a year, and 500 million people in the world face serious water shortage problems throughout the year [4]. How to alleviate this crisis has also become the focus of attention, and now some effective methods have been proposed to collect and utilize the limited fresh water on the earth, such as seawater desalination, atmospheric water harvesting and sewage treatment [5–11]. Based on these, the related research of producing clean water has become a hotspot of modern researchers [12–14].

While freshwater accounts for around 2.5% of Earth's water resources, its proportion has declined in recent years due to pollution and climate change [15,16]. The ocean makes up more than 97% of the total water on the earth, and the atmosphere that surrounds us is also a huge reservoir [17,18]. Extracting fresh water from the atmosphere and seawater is a good choice. On the one hand, water harvesting technologies from the atmosphere include raindrop, dew, and fog collection as well as adsorption [19–25]. In addition, in virtue of the moisture in the air contains less bacteria and impurities, the collected water could be generally ready for further use without complicated sterilization and purification processes [25,26]. Over the past few years, researchers have tried plenty of approaches to optimize the key steps of fog collection including capture of tiny droplets in the air, followed by droplet fusion, transport and final storage [25]. At present, the water in the atmosphere is often collected by modifying the surface wettability or transforming the surface structure and morphology of the material to create biomimetic surface [27–30]. However, due to the relatively low water collection efficiency of planar structure, and the delicate operation of

* Corresponding authors at: Institute for Fiber Engineering (IFES), Interdisciplinary Cluster for Cutting Edge Research (ICCER), Shinshu University, 3-15-1 Tokida, Ueda, Nagano 386-8567, Japan.
E-mail addresses: shi@shinshu-u.ac.jp (J. Shi), morikaw@shinshu-u.ac.jp (H. Morikawa), zhu@shinshu-u.ac.jp (C. Zhu).

https://doi.org/10.1016/j.cej.2023.143330
Received 26 February 2023; Received in revised form 12 April 2023; Accepted 1 May 2023
Available online 5 May 2023

multiple steps are often required during the preliminary design, the production scale is also relatively limited at the same time [29,31].

On the other hand, common seawater desalination technologies include reverse osmosis (RO), multi-stage flash (MSF) desalination and multi-effect distillation (MED) [32]. However, how to carry out relevant researches through the way of carbon neutral and zero carbon is also a difficult problem. In recent years, solar energy, which is widely distributed on the earth and renewable green energy, has been attracted more and more attention [33–36] and leads to development of solar-driven interfacial evaporation [37–43]. One of the most common solar-driven interfacial evaporation materials is photothermal film [44]. There are many studies on photothermal film's solar absorption and anti-pollution properties, however the flexibility and stability of materials have been ignored.

In order to solve these problems related to manufacturing and development mentioned above and to be more effectively developed for multiple scenarios under different conditions, such as the famous Sandwich Bay in Namibia known as the Sand Sea Symphony, which has attracted many researchers, and the frequent fog water is the source of life for this region's flora and fauna [45–48]. Previous studies of clean water production inspired by these creatures have mostly been focused on the collection of fog only, there has been few subsequent research of how to release the water and be not only applied in the desert but also in the ocean nearby [49–51]. In this study, the hydrogel with biomimetic three-dimensional structure and excellent performance which can be formed in one step, is also introduced into a system for producing clean water that can be applied to multiple scenarios.

Selaginella lepidophylla, a remarkable spike moss that can survive desiccation and even resurrect from an air-dried state, undergoes structural changes to adapt to different hydration states [52,53]. Honeycomb structures in nature possess large surface areas, high structural stability, and excellent permeability, which accelerate the directional transport of coalesced tiny droplets and enhance heat and mass transfer for maximal adsorption and desorption rates [28,54–56]. Pufferfish, a common ocean creature, can expand by absorbing water when threatened and return to its original shape when safe, with this transformation being repeatable [57,58]. These three miraculous creatures served as inspiration for the design strategy of a biomimetic and multifunctional hydrogel suitable for producing clean water in various scenarios in this research. In particular, *Selaginella lepidophylla*'s drying resistance and morphological changes resemble the hydrogel's water absorption characteristics, its porous structure is also very similar to that of honeycomb to facilitate water transfer. Furthermore, the water absorption and spitting behavior of pufferfish inspired the hydrogel's water collection and release abilities. The high hydrophilicity, porous, and extensive hydrogen bond network of Polyvinyl alcohol and sodium alginate were utilized, accompanied by borax as a cross-linking agent to prepare functional hydrogels. As a novel polymer material with a three-dimensional network porous structure, hydrogel can make full use of high specific surface area, high porosity and surface activity to endow itself an ideal adsorption agent. The addition of MOFs and graphene not only improve the photothermal property of hydrogel, but also has higher ion adsorption capacity and removal ability of heavy metal ions [59–61]. Hence, it owns high evaporation efficiency, efficacious desalination ability, and durability.

The above advantages make the fabricated hydrogel not only owns the average water harvesting ratio up to 22.44 g g^{-1} under the condition of fog flow after 5 h, but also rapidly release water under solar with water release efficiency of 1.67 kg m^{-2} h^{-1} under 1 sun. Meanwhile, with the help of reasonable and facile devices, it can perform seawater evaporation and desalination more effectively by the synergy to continuously transport seawater to the surface result in the evaporation rate over 1.89 kg m^{-2} h^{-1}. The biomimetic 3D macro/micro/nano hierarchical porous structure of the hydrogel demonstrated in this study ensures rapid water transport and vapor escape. This scalable, modular hydrogel not only triggers new biomimetics ideas and concepts for composite functional material preparation, but also opens a new paradigm for producing clean water in more scenarios in the future as well as good for ecological sustainability.

2. Experimental section

2.1. Materials

Polyvinyl alcohol (PVA, n = 1500 ~ 1800), sodium alginate (SA, 300 ~ 400cP), nitric acid, sodium tetraborate (Borax), cobalt(II) nitrate hexahydrate and methanol were provided by FUJIFILM Wako Pure Chemical Corporation (Japan). Graphene nanoplatelets (6–8 nm thick × 15 μm wide) was obtained from Strem Chemicals, Inc. (USA). 2-Methylimidazole was supplied by Tokyo Chemical Industry Co., Ltd. (Japan). The deionized water was produced by WG250B, Yamato Scientific co., ltd., (Japan).

2.2. Fabrication of ZIF-67 nanocrystal powder

In addition to their ability to provide nano-sized structures, metal–organic frameworks (MOFs) are also well-known for their outstanding adsorption capabilities and photothermal effects. This makes them an ideal component for composite materials with diverse applications. In this study, ZIF-67 was fabricated as one of the functional components in hydrogels. The cobalt(II) nitrate hexahydrate (1.746 g) and 2-methylimidazol (2-MeIM) (1.968 g) were added in 60 mL and 20 mL of methanol separately. Then the $Co(NO_3)_2{\cdot}6H_2O$ solution was added into 2-MeIM solution kept at continuous stirring. The solution was stirred for 10 h at 600 rpm at room temperature (20 ± 2 °C). After that, ZIF-67 nanocrystals were collected by centrifugation at 600 rpm for 20 min and followed by four times methanol washing. The final nanocrystals were then dried in an oven at 60 °C for 12 h.

2.3. Treatment of graphene nanoplatelets

Graphene is a highly effective photothermal material, and its inclusion in the hydrogel can enable the hydrogel to release water under sunlight, akin to the way a pufferfish expels water. This property can be attributed to the excellent photothermal effect of graphene, which generates heat under sunlight and results in water being released from the hydrogel. To make graphene nanoplatelets more easily dispersed in the solution subsequently, graphene nanoplatelets (0.5 g) and nitric acid solution (50 mL, 3 mol L^{-1}) were mixed and stirred for 14 h at 100 °C at 300 rpm. After acidification, the graphene solution was cooled to room temperature and washed repeatedly with distilled water until the solution become neutral. It was finally put into the oven and dried at 45 °C for 12 h.

2.4. Preparation of different types of PVA/SA based hydrogels

A hydrogel matrix was chosen as the most suitable material to mimic the different states of *Selaginella lepidophylla*. To create the hydrogel, PVA and SA were utilized as the primary matrix components. PVA powder was dissolved in deionized water (10 wt%) at ~ 85 °C with continuous stirring for 4 h. The 3.5 wt% SA solution was prepared under the same condition. Different mass ratios of 1:2, 1:1 and 2:1 PVA/SA solutions were poured into beakers respectively, kept stirring at 80 °C for 3 h, then poured into molds. 10 wt% borax solution was dripped onto the PVA/SA solution, accompanied by keeping the mass ratio of PVA/SA solution to borax solution at 3:2. After being crosslinked 12 h at room temperature, the original PVA/SA hydrogel (PVA/SA) was obtained. Graphene nanoplatelets and ZIF-67 and the mixture of the two (1:1) were added into the PVA/SA solution at a ratio of 1 wt% separately, and kept vigorous stirring at 80 °C for 4 h. Graphene/PVA/SA hydrogel, ZIF-67/PVA/SA hydrogel and graphene/ZIF-67/PVA/SA hydrogel (GZPS) were prepared according to the preparation method as same as the

original PVA/SA hydrogel mentioned above.

2.5. Vacuum freeze-drying treatment for as-prepared hydrogels

Freeze-drying was utilized in this study to create a honeycomb-like porous structure in the hydrogel matrix. Liquid nitrogen was slowly poured into the paper cups that have been filled with four different hydrogels prepared before, so that the hydrogels can be quickly frozen in a short time to maintain their porous structure. Next, the frozen hydrogels (PVA/SA hydrogel, graphene/PVA/SA hydrogel, ZIF-67/PVA/SA hydrogel and graphene/ZIF-67/PVA/SA hydrogel were vacuum freeze-dried for 24 h. The obtained biomimetic aerogels with honeycomb structure were called PVA/SA, graphene/PVA/SA, ZIF-67/PVA/SA and GZPS respectively.

2.6. Instruments and characterization

Morphological investigation was analyzed by using a field emission scanning electron microscope (FE-SEM, S-5000, Hitachi High-Tech Corporation, Japan). Element composition and distribution of the samples were analyzed by using a scanning electron microscope (SEM) equipped with an energy-dispersive spectroscopy (EDS) device (SEM, JSM-6010LA, JEOL Ltd., Japan). Before the morphological investigation, a layer of gold was spurted onto samples' surface to prevent the accumulation of electrons by auto fine coater (JFC-1600, JEOL Ltd., Japan). The mechanical property test was carried out using a tensile tester (MCT-2150, A&D, Japan). TG-DTA curves was obtained by thermo gravimetry analyzer (TG8120, Rigaku, Japan). The viscoelasticity of the sample was tested by dynamic viscoelasticity measuring device (DVA-225, itkdva, Japan). The chemical component was recorded by utilizing Attenuated total reflectance-Fourier transform infrared (ATR-FTIR) (FT/IR-6600•IRT-5200, JASCO Corporation, Japan). The X-ray diffraction (XRD) patterns were recorded with a diffractometer (MiniFlex300, Rigaku Corporation and its Global Subsidiaries, Japan). X-ray photoelectron spectroscopy (XPS) analyses were performed using an X-ray photoelectron spectrometer (AXIS-ULTRA HAS SV, Kratos Analytical Ltd., Japan). UV–vis–NIR spectra was measured by a Shimadzu UV-3600 spectrophotometer (MPC-3100, SHIMADZU CORPORATION, Japan). Static water contact angles (WCA) were measured ten times on the different points of each sample by an automatic contact angle meter (DMs-400, Kyowa Interface Science Co., Ltd., Japan) at room temperature 20 ± 2 °C with a 1 μL droplet each time. The temperature infrared images were recorded by a FLIR thermal imaging camera. The ions' concentrations in natural seawater and the collected water were determined with the help of ICP emission spectroscopic analyzer (SPS3100, Hitachi High-Tech Science Corporation, Japan).

2.7. Water harvesting and release assessments

The mass of the aerogel was recorded before the fog absorption experiments. The ambient temperature is 20 ± 2 °C and the relative humidity is 45 ± 5 %RH. The humidifier (HTJS-007 J-WH, MODERN DECO Co., Ltd., Japan) provided a fog flow was placed 15 cm away from the tested aerogel. To facilitate long-term water collection, a facile aerogel water collection device was settled up, and the detailed structure can refer to the Fig. S1. The whole fog-harvesting device was placed on the electronic balance (GR-200, A&D Company, Japan) and the real-time fog-harvesting mass were recorded. Simultaneously, to exclude the interference of other factors, and the device without aerogel was also tested for water collection. Finally, the results of each hydrogel water harvesting trend were also subtracted from the blank control group to obtain the results of water uptake by the hydrogel water harvesting device.

The water uptake rate (W_u) and water harvesting ratio (R_h) can be calculated by the following equations (Eqs. (1) and (2)):

$$W_u = \frac{m_1 - m_0}{m_1} \times 100\% \tag{1}$$

$$R_h = \frac{m_1 - m_0}{m_0} \tag{2}$$

where m_0 is the mass of the initial mass of the hydrogel before the water harvesting behavior (g), m_1 is the mass of the current mass of the water harvesting system (g) (after removing the water harvesting mass of the blank device).

The water release experiment was performed at 20 ± 2 °C and 45 ± 5% RH, accompanied by being exposed to solar simulator (XES-40S3-TT, SAN-EI Electric, Japan) of 1 sun irradiation. The mass of the irradiated hydrogel was recorded by the weighing system in real time. Water release unit gram mass (W_r) and water release efficiency (η_r) were obtained by calculation through the following equations (Eqs. (3), (4)), respectively:

$$W_r = \frac{m_b - m_a}{S_r} \tag{3}$$

$$\eta_r = \frac{W_r}{t} \tag{4}$$

where m_a is the mass of the initial mass of the hydrogel before the water release behavior (kg), m_b is the mass of the current mass of the hydrogel (kg). t is the irradiation time (h), S_r is the area of the irradiated top surface of the hydrogel (m^2).

2.8. Preparation of the solar-driven seawater evaporation device system and performance measurements

In order to enhance the evaporation effect of the hydrogel based on previous related researches, a proper evaporation system was adopted [29,44]. In order to distinguish materials in different hydration states, PVA/SA, graphene/PVA/SA, ZIF-67/PVA/SA and GZPS aerogel after water harvesting were labeled as PVA/SA gel, graphene/PVA/SA gel, ZIF-67/PVA/SA gel and GZPS gel. The gel was taken as solar irradiation functional absorber, the polystyrene foam was applied as the thermal insulation and seawater-trapped layer, cotton was used as a channel to transport seawater. In subsequent experiments, the device system without the gel was also tested to determine the role of the solar irradiation absorber in solar-driven water collection and release.

The device system was applied for the following solar-driven evaporation and desalination experiments under the simulated 1 sun. The real-time mass and temperature changes were recorded during the evaporation experiment. The water evaporation mass change per area (Δm_e), evaporation rate (R_e) and solar-thermal conversion efficiency (η_e) can be calculated by the following equations (Eqs. (5), (6) and (7)):

$$\Delta m_e = m_a - m_\beta \tag{5}$$

$$R_e = \frac{\Delta m_e}{S_e T} \tag{6}$$

$$\eta_e = \frac{(R_{e1} - R_{e0})h_v}{C_{opt} P_0} \tag{7}$$

where m_a refers to the current mass of the whole evaporation device (kg), m_β is the mass of whole evaporation device before evaporation (kg). S_e is the area of the top evaporation surface of the hydrogel (m^2), and T is the solar evaporation time (h). where R_{e1} represents the solar-driven evaporation rate, R_{e0} is the dark natural evaporation rate, h_v donates to the liquid–vapor phase transition enthalpy, C_{opt} is the optical density, and P_0 donates to the power density of 1 sun radiation.

3. Results and discussion

3.1. Design and synthesis of biomimetic hydrogel

Bioinspired by the hydro-responsive behavior and morphological changes of *Selaginella lepidophylla* at various hydration states, as well as the hierarchical capillary water-collecting structure of honeycomb and the ability of pufferfish to absorb water, expand, and release water to shrink, the concept of biomimetic composite hydrogel was developed in this study has been proposed. As mentioned above, the water response behavior and morphological changes of *Selaginella lepidophylla* in different hydration states and the hierarchical capillary porous structure of the honeycomb that is conducive to water transmission and the use of polyvinyl alcohol and sodium alginate supplemented with borax as a cross-linker. The properties of the functional hydrogel matrix prepared by the agent are very close. In addition, the addition of ZIF-67 and graphene will make the hydrogel have the performance of photothermal conversion, so that the composite hydrogel can release water and improve evaporation performance. This bioinspired composite hydrogel owns a macro/micro/nano hierarchical structure and is capable of producing clean water in various scenarios and under different water conditions. (Fig. 1a).

The main matrix materials of hydrogels are PVA and SA. To determine the appropriate ratio of PVA to SA and the minimum amount of cross-linking agent required, the physical fluid gel PVA/SA in different mass ratios (1:2, 1:1, 2:1) that have been thoroughly mixed before were prepared. The same mass of borax solution was dropped to the pre-gel solutions' surfaces. After the cross-linking reaction overnight, the state of the gels with three ratios is shown in Fig. S2. From the states of the cross-linked hydrogels, it can be seen that the 1:2 pre-gel still presents a very strong fluid state. When the ratio is 1:1, although it has reached the cross-linked state, the degree of cross-linking in some areas with bubbles is not sufficient. Finally, the ratio of PVA/SA of 2:1 was used for subsequent preparation and applications. Fig. 1b shows the specific details of the biomimetic hydrogel preparation process, using GZPS as an example. To investigate the effect of added functional nanomaterials,

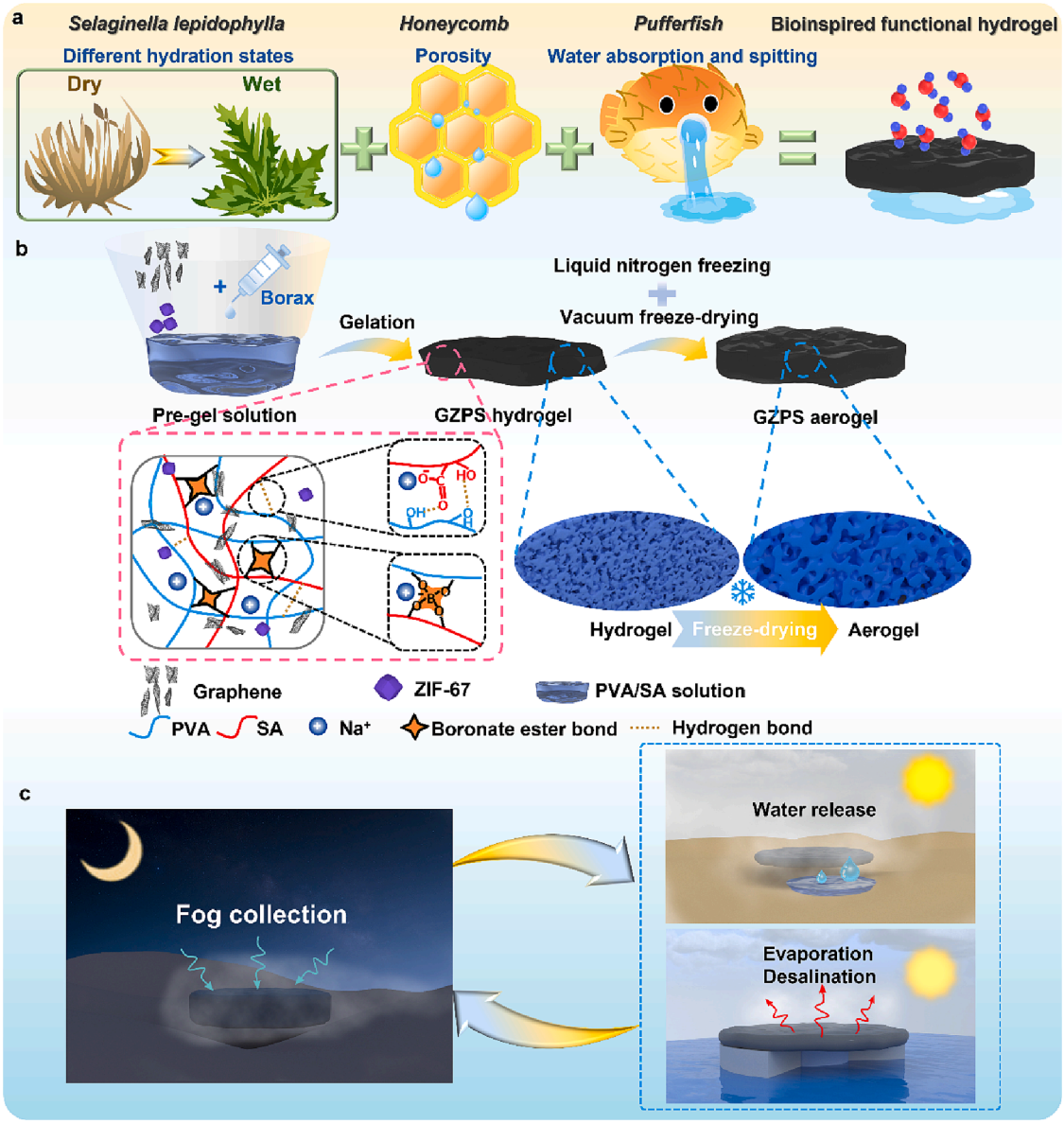

Fig. 1. Multi-bioinspired design and conceptual representation for the multi-functional hydrogel. (a) Scheme of integrating the features of the *Selaginella lepidophylla*, pufferfish and honeycomb to inspire the fabrication of hydrogel. (b) A flow chart of fabrication of GZPS hydrogels. (c) Schematic illustration of water harvesting, water release and solar-driven evaporation.

four types of hydrogels were prepared: PVA/SA hydrogel without any added pre-gel, PVA/SA hydrogel with only graphene, PVA/SA hydrogel with only ZIF-67, and pre-gels added with both. At the same time, the chemical mechanism has also been elucidated. The − OH groups in PVA and SA reacted with tetrahydroxyborate anions ($B(OH)_4^-$) and formed bis(diol)–borax complexes as cross-linking points, then formed an interpenetrating polymer network hydrogel. The fabricated hydrogels were pre-frozen to maintain the porous state and then vacuum freeze-dried to enable the formation of a complete hierarchical porous structure. Specifically for its application, this hydrogel can effectively collect the fog when there is a fog flow in the surroundings in its dry state. After collecting water, it can release the water collected under solar irradiation. Simultaneously, it could also be applied in its wet state wet state for solar-driven seawater desalination (Fig. 1c). All of these functions in different scenarios can be applied to produce clean water.

3.2. Appearance, performance characteristics and microscopic hierarchical structure of functionalized hydrogels

Fig. 2a shows that the original PVA/SA hydrogel dyed with edible red and blue pigments, undyed hydrogel and GZPS hydrogels can be molded into various shapes, showing its softness and moldable, which can be used according to different scenarios or assembled containers. Fig. 2b and Fig. S3 demonstrate the self-healing properties of hydrogels, even after being stretched, twisted, frozen and thawed, as well as chopped.

These phenomena can be attributed to the reversible boronic ester bonds and the bis(diol)-borax complexation went through the PVA and SA networks, forming reversible dynamic covalent bonds, which made the PVA/SA-based hydrogels own self-healing properties [17]. The appearance of small-sized aerogels formed after pre-frozen and vacuum freeze-drying have been shown in Fig. 2c and Fig. S4, and the lightweight characteristic can be seen in Fig. 2d. It further hinted that it can be easily carried and applied at anhydrous state. The morphology and EDS distribution of self-made ZIF-67 nanocrystal powder and treated graphene are shown in Figs. S5 and S6. Fig. 2e-l show the morphological structures of four aerogels. It can be observed that all four hydrogels have a honeycomb-like structure and a macro/micro/nano hierarchical structure. This peculiar macro-porous structure owning dense graded microstructure will affect the photothermal effect, steam escape, water transport performance and salt diffusion [62]. No matter whether the functional nanomaterials were added or not, the biomimetic structure of the honeycomb were not be affected. Graphene possesses multi-layers sheet structure, so it cannot be directly observed on the Graphene/PVA/SA skeleton structure. On the contrary, ZIF-67 could be clearly observed which are marked in purple (enlarged views inserted in Fig. 2k, l). EDS distribution of Fig. 2m-q and Fig. S7a-h exhibit that B, C, O, and Na elements evenly distributed in each hydrogel at the microstructure level, and Co element also appeared uniformly in the added hydrogel of ZIF-67, which means each component material was uniformly distributed throughout the hydrogel and formed a network structure. Strategies such as multi-hierarchical structure can maintain stable evaporation rate and inhibit salt precipitation [62]. In addition to demonstrating the water absorption and release properties of the GZPS gel, it is also

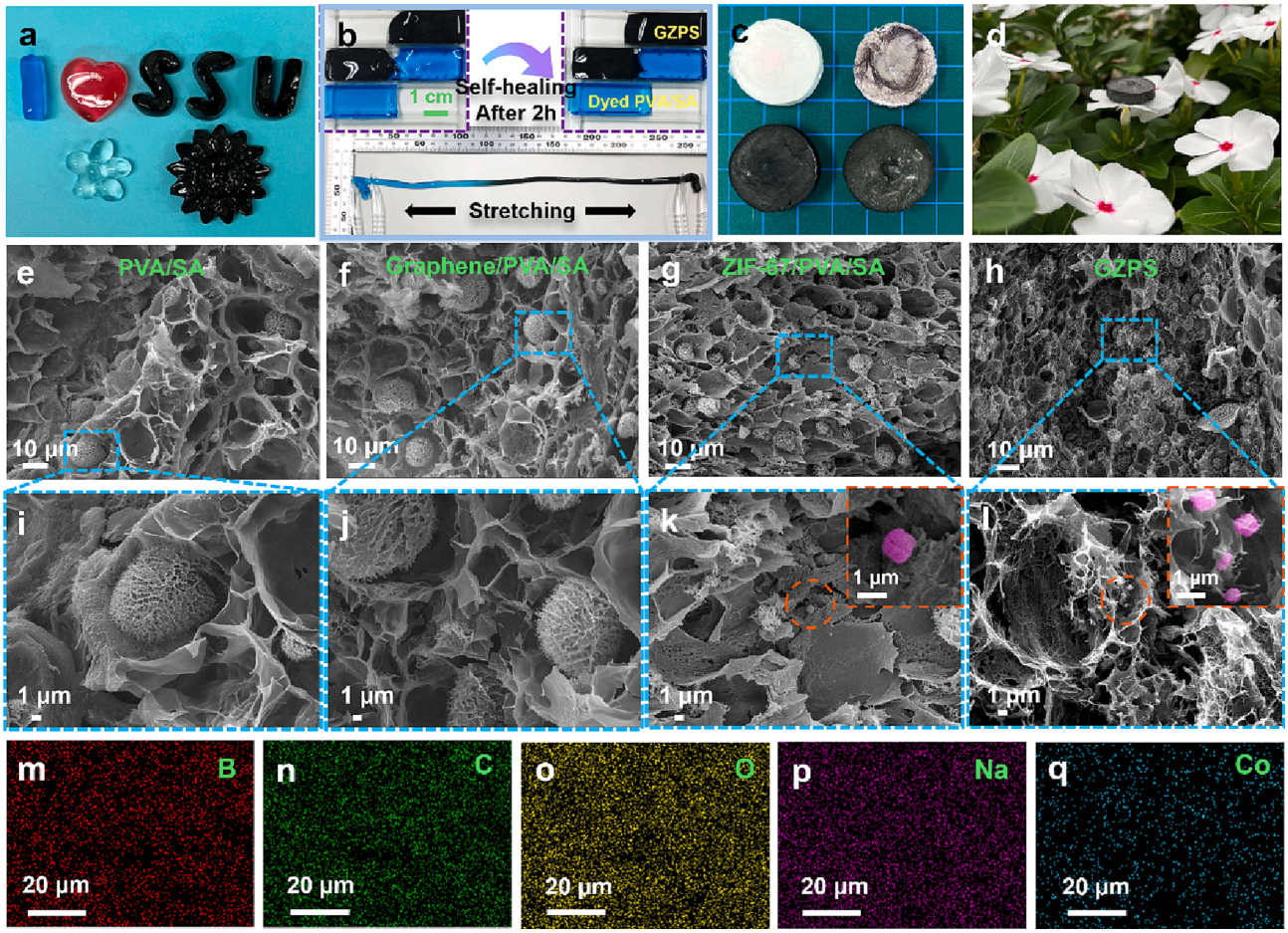

Fig. 2. Appearance, microstructure and element distribution of hydrogels. (a) Different fabricated hydrogels of various shapes. (b) Self-healing behavior of hydrogels. (c) Small-sized aerogels' appearances, and the lightweight demonstration (d). (e-l) FE-SEM images of different aerogels. The corresponding enlarged images inserted reveal hierarchical biomimetic structures. (m-q) Elemental distribution on GZPS hydrogels.

important to evaluate its mechanical properties, as they are crucial for its practical application. In Fig. S8a and b, the tensile stress–strain curve and 50 cyclic compressive loading/unloading cycles of the GZPS gel were shown, respectively. Furthermore, dynamic rheological testing was also performed on the GZPS gel (Fig. S8c), which showed its viscoelastic properties.

3.3. Chemical composition and surface wettability of hydrogels in different hydration states

Chemical structures and compositions of the four hydrogels were characterized, and the results are presented in Fig. 3 and Figs. S9–S11. FTIR spectra in Fig. 3a and Fig. S9 demonstrate the chemical components of hydrogels. The broad peak at 3502 cm^{-1} corresponds to the stretching vibration of O − H. The peak at 1356 cm^{-1} is the characteristic absorption peak of the B − O group from borax. Broad absorption bands at 3200–3600 cm^{-1} corresponding to the O − H stretching vibrations from the − OH groups of PVA and SA were found in four different hydrogels. The sharp peaks at 1027 cm^{-1} and 1600 cm^{-1} correspond to the C − O stretching vibration of the − COOH groups and the symmetric stretching vibration of the C − O − C linkages of SA.

The characteristic peaks of borax, PVA, and SA were observed in all four hydrogels, implying that these materials' components were incorporated into the hydrogels successfully [63]. Further, in order to confirm that ZIF-67 was successfully introduced, XRD characterization was introduced (Fig. 3b, S10), and the characteristic diffraction peaks of other substances were indeed not observed in the original PVA/SA without any functional nanomaterials being added. The characteristic diffraction peak of graphene appears in both graphene/PVA/SA and GZPS, and the characteristic peaks of ZIF-67 nanocrystal powder also appears in ZIF-67/PVA/SA, but the characteristic peak of graphene was not obvious, so the XPS was relatively sensitive to perform analysis on GZPS, it can be deduced that GZPS has successfully incorporated graphene and ZIF-67 from its scanned full spectrum as well as the full surveys of added graphene and ZIF-67 (Fig. 3c, S11).

Considering that the surface wettability of prepared hydrogels in different hydration status has a great influence on the fog collection performance and seawater evaporation, [49,64] the water contact angles of the samples were measured. Each sample was tested ten times at different positions on the surface, and since the samples were found to be hydrophilic and swiftly absorbed 1 μL of testing water droplets, WCAs of the samples at 100 ms were recorded, and the average value and standard deviation were calculated.

From Fig. 3d, it can be found that the four aerogels formed by freeze-drying are all hydrophilic, and the average WCA of GZPS in the aerogel state is 42.4°. The aerogels with hydrophilicity are also conducive to the subsequent water collection effect. Furthermore, after becoming wet during the water harvesting experiment, the WCAs became smaller, leading to the surface of the substrate of material more hydrophilic. As a result, the average WCA of GZPS gel is reduced to 13.3°. The hydrophilic matrix can ensure that the surface of the gel material will be more hydrophilic during evaporation, which is beneficial to fast water transfer to the evaporation surface as well as facilitates the diffusion of salts to reduce the impact of salt precipitation on seawater evaporation efficiency thus improving lifespan and solar-to-steam conversion efficiency.

3.4. Photothermal conversion properties of hydrogels in different hydration states

The excellent photothermal performance of the hydrogel matrix is not only conducive to the subsequent water release but also beneficial to the evaporation and desalination of seawater driven by solar. Graphene

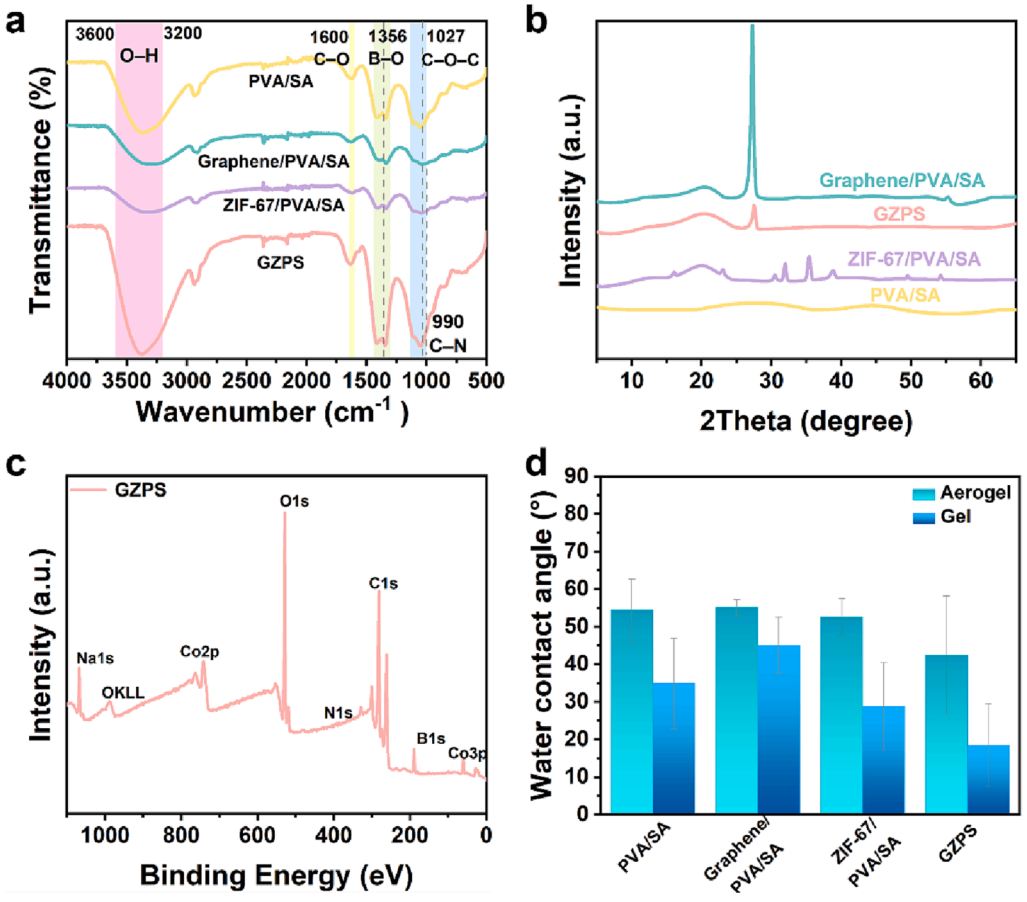

Fig. 3. (a) FTIR spectra, (b) XRD patterns of all samples, (c) survey XPS spectra of GZPS, and (d) Static WCAs of hydrogels in different hydration states.

and ZIF-67 were introduced into the hydrogel matrix because of their excellent photothermal performance and adsorption capacity, [65] while ZIF-67 is also often exploited in water treatment, visible light-driven catalysis and thermal decomposition applications [66].

The aerogel nearly contains no water, however it would be filled with water after the water harvesting experiment. These two states (dry and wet) lead to corresponding influences and differences on the solar-to-heat conversion performance. With the intention of exploring the performance of solar-heat conversion, the temperature changes of the four kinds of aerogels and the aerogels after being implemented the water harvesting processes were monitored under 1 sun, when the ambient temperature is 20 ± 2 °C and the relative humidity is 65 ± 5%. According to Fig. 4a, although the temperature of PVA/SA aerogel rose slightly only to 32.4 °C within 10 min, the graphene/PVA/SA rose to 54.8 °C because of the addition of graphene, the solar-heat conversion ability has been significantly improved. Although the ZIF-67/PVA/SA aerogel rose to 47.8 °C, the GZPS aerogel with the same total mass ratio of the added functionalized nanomaterials with the ratio of graphene:ZIF-67 (1:1) could also rise to 54.7 °C in 10 min, which indicating that even if the amount of added graphene of GZPS was reduced to only half compared to the graphene/PVA/SA also been given the synergistic photothermal effect of ZIF-67. GZPS aerogel maintains good solar-heat conversion ability, and the synergistic effect of ZIF-67 and graphene accelerates the temperature change of GZPS. Fig. S12 directly demonstrates the infrared imaging of surface temperature of four kinds of aerogels under 1 sun.

To verify whether the hydrogel molded into other irregular shapes could also maintain excellent solar-heat conversion performance, it was shaped like a flower. The flower-shaped one was also tested for light-heat conversion. It was found that the flower-shaped GZPS aerogel can also exhibit almost consistent temperature changes under solar radiation within 10 min (Fig. 4b). The composite aerogel owns stable photothermal conversion performance no matter what shape it is. While maintaining the room temperature, when the external humidity was changed to 40 ± 5 °C, the cycle experiments with or without solar irradiation (Fig. 4c) also proved its excellent photothermal conversion performance and implied that it can be utilized when the ambient humidity is lower, leading to photothermal effect even be better represented.

In addition to the excellent photothermal performance of the fabricated material in dry state without moisture, which proves that it can effectively absorb solar energy, whether it still has excellent photothermal conversion ability after the water harvesting is still worth being checked. After the water collection behavior of the four aerogels, similar characterization experiments were carried out to explore the solar-heat conversion capabilities of the four gels in the wet state. The full band absorption performance of four kinds of gels was investigated by the UV–vis–NIR spectrum. As shown in Fig. 4d, PVA/SA gel reflects the worst absorption of solar light. However, neither with the addition of ZIF-67 or graphene or both, the totality solar light absorption rate is significantly improved, showing full-band absorption range from 300 nm to 2500 nm, thanks to ZIF-67 as well as the efficient photothermal conversion of graphene. It also proves that graphene/PVA/SA gel, ZIF-67/PVA/SA gel and GZPS gel can absorb sunlight effectively. Meanwhile, the solar absorption efficiency of the GZPS gel was calculated to be 95.25%, demonstrating its superior solar absorption capability. The temperature of the four gels all increased within 30 min under the solar radiation (Fig. 4e). When the simulated sunlight was turned on, the temperature rose rapidly, then the temperature increased slowly after 10 min. Considering that the gels were in the state of being irradiated by solar light, the water in the matrix was evaporated and absorbed heat from the matrix, the gels were taken away part of the heat. The upper limit temperature will be much lower than that of aerogel when it was dry, however graphene/PVA/SA gel and GZPS gel still maintain proper

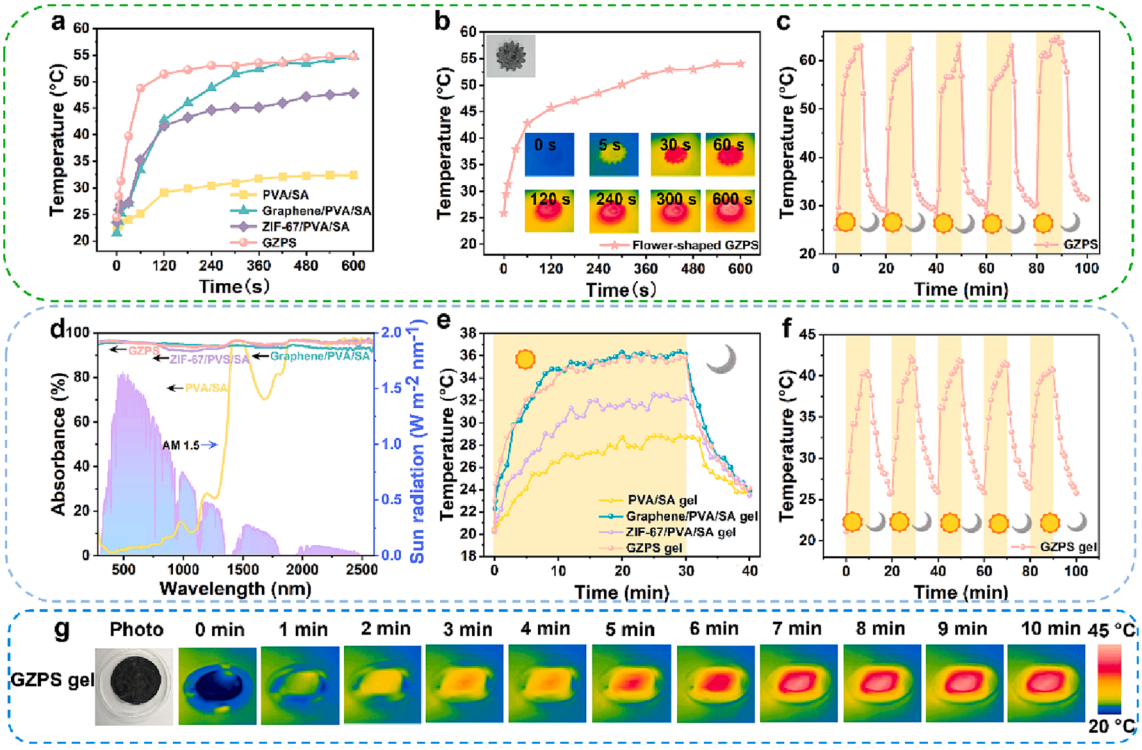

Fig. 4. Solar-heat conversion properties of hydrogels in different hydration states. (a) Surface temperature change of four kinds of aerogels (PVA/SA, graphene/PVA/SA, ZIF-67/PVA/SA, GZPS) under 1 sun. (b) Surface temperature change of flower-shaped GZPS aerogel under 1 sun with the IR images inserted. (c) The temperature curves of photothermal cycle test for GZPS aerogel. (d) The UV–vis-NIR spectra of four gels (PVA/SA, graphene/PVA/SA, ZIF-67/PVA/SA, GZPS). (e)Surface temperature change of four kinds of gels under 1 sun and in dark. (f) The temperature curves of photothermal cycle test for GZPS gel under 1sun. (g) IR images of GZPS gel under 1 sun irradiation at various time points.

photothermal conversion capabilities, both reached about 36.4 °C. Correspondingly, when there is no light source the temperature of the gels would also decline rapidly, demonstrating its ability to respond rapidly to solar heat. In addition, the cycle photothermal test performed on GZPS gel showed its high photostability and stable energy conversion ability (Fig. 4f). Fig. 4g directly shows the temperature distribution and temperature change of GZPS gel when it was irradiated by solar light during the cycle test. The results above indicate that the hydrogels added with graphene and ZIF-67 own good solar-heat conversion ability in both dry and wet states and can be utilized as desorption host materials for collected water and efficient solar absorbers for interfacial solar driven evaporation.

3.5. Water harvesting and release performance

Four kinds of aerogels that have been fabricated were utilized to explore their water absorption and water release ability, the schematic diagram of the experimental setup is shown in Fig. 5a. The fog flow velocity is 50–70 cm s^{-1} (tested by an anemometer, Model 6541-01, KANOMAX, Japan). After a period of water collection experiment, the gel enriched with collected water was placed under simulated sunlight. The desorption behavior was monitored, and its temperature change and real-time mass change were also recorded simultaneously. Regarding the water absorption capacity, two calculation methods are adopted to measure their water harvesting capacity. First, according to the Eq. (1), the ratio value of the real-time change mass to the real-time total mass (i.e., dry hydrogel mass plus collected water mass) can be used to measure the degree of water uptake, that is, the moisture content of the material overall. From Fig. 5b, it is evident that all four aerogels were capable of effectively collecting water. However, PVA/SA hydrogel only captures water molecules through the matrix containing hydrophilic groups, resulting in a water uptake rate of only 78.73% after 3 h of water collection behavior. However, after adding the functional nanomaterials containing hydrophilic groups, the water uptake ratio of the hydrogel containing both of graphene and ZIF-67 reached 94.06% after a 3 h water harvesting test, which proved its relatively high-water content.

According to Eq. (2), the mass of the aerogel when it did not contain water was used to measure how much water can be harvested per unit mass of the aerogel (Fig. 5c). It can be seen intuitively that GZPS aerogel continued to harvest water within 3 h with the cooperation of a facile water collection device, the water harvesting ratio can reach 15.84 g g^{-1}, which is the highest among the four samples. In order to test whether GZPS aerogel possesses stable and excellent water harvesting characteristics and fabricating repeatability, ten GZPS aerogels produced at different times were subjected to water harvesting experiments, the experiment time was also extended to 5 h (Fig. 5d). The water uptake

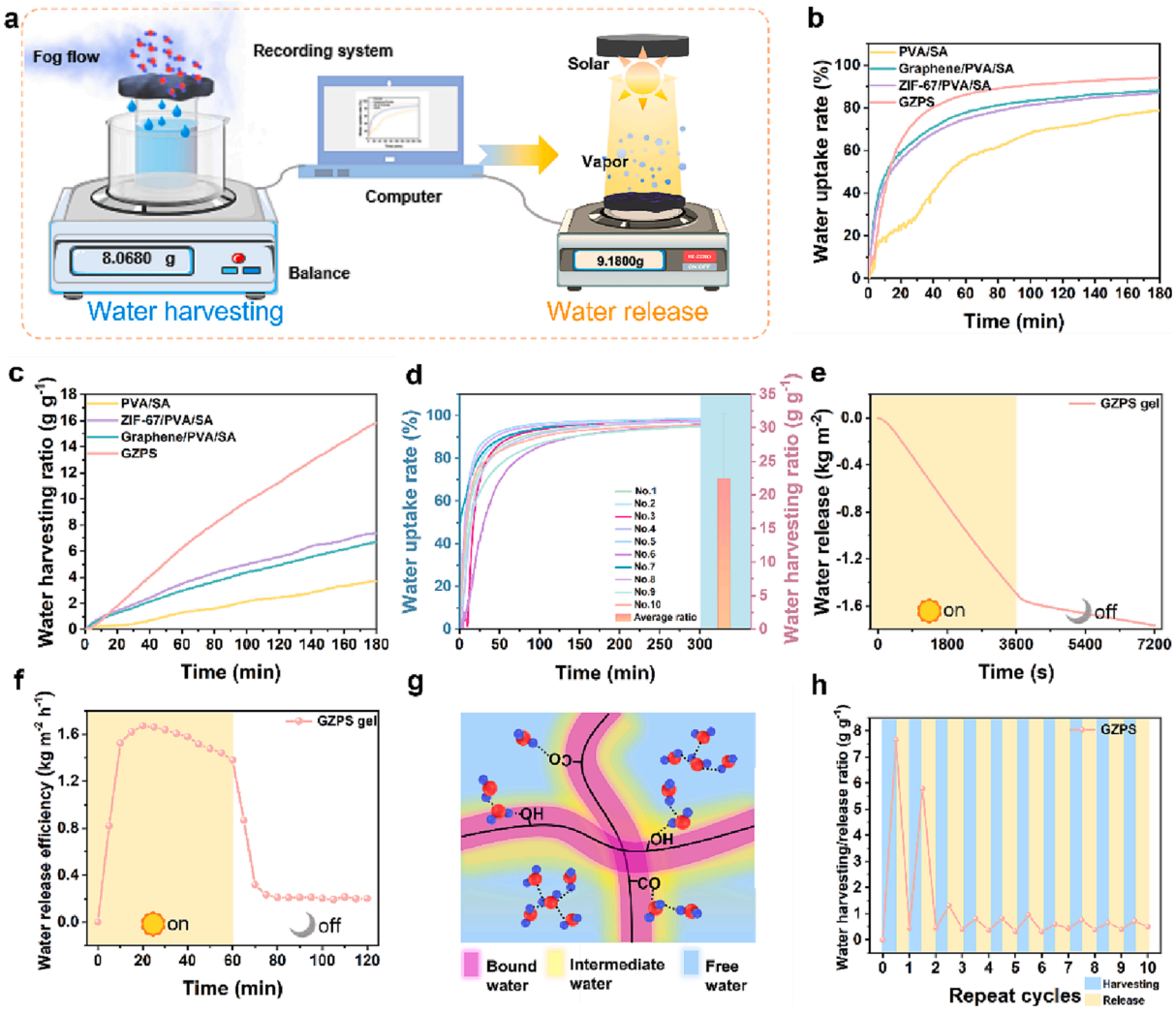

Fig. 5. Water harvesting and release behaviors. (a) Schematic diagram of the water harvesting and release experiments. (b) Water uptake rate change and (c) water harvesting ratio change of four aerogels during the 3 h water harvesting test. (d) Water harvesting performance of 10 GZPS aerogels during 5 h water collection tests. (e) Water release change of per unit area and water release efficiency (f) of GZPS gel under 1 sun or in the dark. (g) Schematic illustrating different water types-bound water, free water, and intermediate water in the hydrogel. (h) Continuous water harvesting and release cycle tests.

ratio of different ten batches of the GZPS aerogels could reach above 95% approximately after 5 h, and the average water harvesting ratio even reached 22.45 g g^{-1}, which shows its excellent water absorption ability. Henceforth, only the GZPS series hydrogels were applied for the subsequent water release experiments and the following solar-driven seawater evaporation experiment.

The gels that have collected water were placed under simulated sunlight to explore their water release performance. According to Eq. (3), the water released per unit area of the irradiated gel under 1 sun is calculated over time. From the cumulative mass change (Fig. 5e), it is apparent that the GZPS gel can release water rapidly in response to solar radiation, and the amount of released water significantly reduces in the absence of radiation. The real-time water release efficiency every 5 min (Fig. 5f) was also obtained according to the Eq. (6). Under solar radiation, the GZPS gel exhibited rapid water release with a maximum efficiency of about 1.67 kg m^{-2} h^{-1}. Although the efficiency decreased with the prolonged radiation time, it remained relatively high, possibly due to the hydration effect (Fig. 5g). The polymer chains in the hydrogel can capture nearby water molecules by interactions such as hydrogen bonds to form bound water, while water molecules separated from the polymer chains are free water, presenting same properties with those in bulk water. The intermediate area between bound water and free water owns intermediate water. This kind of intermediate water is considered as activated water which can be evaporated with less energy than bulk water [67]. Therefore, it is speculated that the activated water in the hydrogel should be evaporated firstly. As the evaporation time was prolonged, the remaining bound water and free water could not be easily evaporated, so the efficiency was reduced over time. However, relying on the excellent photothermal properties of graphene and ZIF-67 enabled it still release water under solar radiation. At the same time, to investigate the sustainability of its water harvesting and release efficiency, continuous cycle experiments were conducted. The experiment involved passive water collection for 3 h and solar-driven water release for 1 h, which was considered as one cycle (as shown in Fig. 5h). The mass of the hydrogel was measured during each cycle to compare the water collection and release characteristics of the material. The unit weight was calculated based on the hydrogel matrix itself, without the aid of any additional device, to provide a more intuitive comparison. The calculation was based on the initial mass of each experiment of dry gel (for harvesting) or wet gel (for releasing). It can be seen that the water harvesting efficiency is relatively high at the beginning due to the aerogel state, which can reach 7.66 g g^{-1}. The water release ratio maintained at the same level, but as the number of cycles increases, its water absorption capacity decreased. This may due to the water release time of 1 h is not enough to release the all collected water, when the inside space of the gel is filled with water, the water collection ratio will be lower than when it starts to collect water in a dry state. As the number of cycle experiments increased, the GZPS gel was able to maintain a relatively stable water harvesting and release performance, even when it already contained water. To provide a more intuitive comparison with the original aerogel, the mass of water released by the GZPS gel was also calculated and plotted as a negative value against the weight of the original dry gel (Fig. S13). The fluctuations in a certain range prove its coherence, stability and durability in water harvesting and release. These behaviors and performance can be attributed to the synergistic effect of the hydrogel matrix and the added ZIF-67 and graphene. By utilizing bionic structures (porous structures similar to honeycombs) and characteristics (*Selaginella lepidophylla*'s ability to adapt to different conditions), the gel was fabricated to mimic the water absorption and spitting behavior of pufferfish. This achievement demonstrates the potential of biomimetic and multifunctional hydrogels for producing clean water in a variety of scenarios. The stable water harvesting and release performance of the GZPS gel, even after repeated cycle experiments, suggests that the material has good durability and can withstand long-term use, making it a promising candidate for practical applications. At the same time, a simple self-healing test on GZPS gel in different states was conducted. The GZPS aerogel with cracks in the dry state even could recover a certain degree of self-healing effect after water collection for 4 h (Fig. S14).

3.6. Solar-driven seawater evaporation performance

The excellent water transmission performance of GZPS gel can ensure the interfacial evaporation when it is driven by solar energy. On the other hand, its internal biomimetic porous hierarchical structure can also ensure the smooth passage of steam and effective desalination to purify seawater [62]. The schematic diagram of the seawater evaporation experimental device and recording concept system is shown in Fig. 6a. To fully exert the function of the prepared hydrogel and prolong the service life, according to some previous studies [29,37,44], the specific appearance of the evaporator device system is shown in Fig. 6b. It shows that hydrogel is used as the uppermost solar absorber to convert the absorbed sunlight into heat energy to drive seawater evaporation. The thickness of GZPS is 5×10^{-3} m, the diameter is 5×10^{-2} m, and the surface area is about 1.9625×10^{-3} m^2. Polystyrene foam is applied as a heat insulation layer, and a cotton piece is inserted in the middle as seawater supply channel. When the entire facile evaporation device floats on the sea surface, seawater can be directly and effectively transported to the upper GPZS gel. Accompanied by proper heat management, GZPS can perform considerable evaporation potential. This entire device is called GZPS device system. For the sake of comparing the effectiveness of the GZPS in seawater evaporation, only natural seawater (from the Sea of Japan, Kamakura City, Kanagawa Prefecture, Japan, the coordinate of latitude and longitude is 35.30487°N, 139.50995°E)), seawater configured with only the device system without GZPS and GZPS device system were used for seawater evaporation experiments. The temperature change IR images can be seen from Fig. 6c. Correspondingly, the temperature change curves of 1 h radiation were also shown in Fig. 6d. The temperature of the GZPS gel in the GZPS device system reaches about 42.5 °C, the surface temperature of the device system is 33.1 °C, and the natural seawater is 28.5 °C after 1 h. The results exhibit that the heat of solar radiation on the interface of the GZPS device system evaporator is significantly more concentrated than the other two, which can reduce unnecessary heat loss and improve energy utilization efficiency, thus promoting the efficient generation of solar steam. The mass change of GZPS device system, device system and natural seawater over time under different conditions is shown in Fig. 6e. The natural seawater and device system are only 0.31 and 0.38 kg m^{-2} h^{-1} under 1 sun, but the GZPS device system is 1.34 kg m^{-2} h^{-1}, three times higher than the natural seawater and device system. The GZPS device system, device system and natural seawater were tested continuously under the condition of the simulated sunlight being switched on and off (Fig. 6f). It can be found that the evaporation speed of these three evaporation systems is faster under sunlight than dark condition, proving that the strong broadband absorption ability of GZPS gel can effectively promote the evaporation of seawater by solar. Then the corresponding real-time evaporation efficiency and solar thermal conversion efficiency during each five minutes were calculated according to the Eqs. (6) and (7), respectively (Fig. 6g). The evaporation efficiency of GZPS device system can reach 1.47 kg m^{-2} h^{-1}, and its solar thermal conversion efficiency even reached 92.32%, while the highest evaporation efficiency of natural seawater and device system without GZPS gel is only 0.44 and 0.55 kg m^{-2} h^{-1}, respectively, and the solar thermal conversion efficiency is only 18.91% and 30.67%, respectively. Comparing these three evaporation behaviors, GZPS device system achieves satisfactory solar steam generation rate and efficiency. It should be noted that in such calculation steps, the energy loss like convection with air (q_{conv}), radiation to the environment (q_{rad}), and conduction to underlying bulk water (q_{cond}) was ignored [36]. By taking all the energy loss as well as the sunlight reflection and transmission into account, the energy efficiency is determined. (See detailed calculation

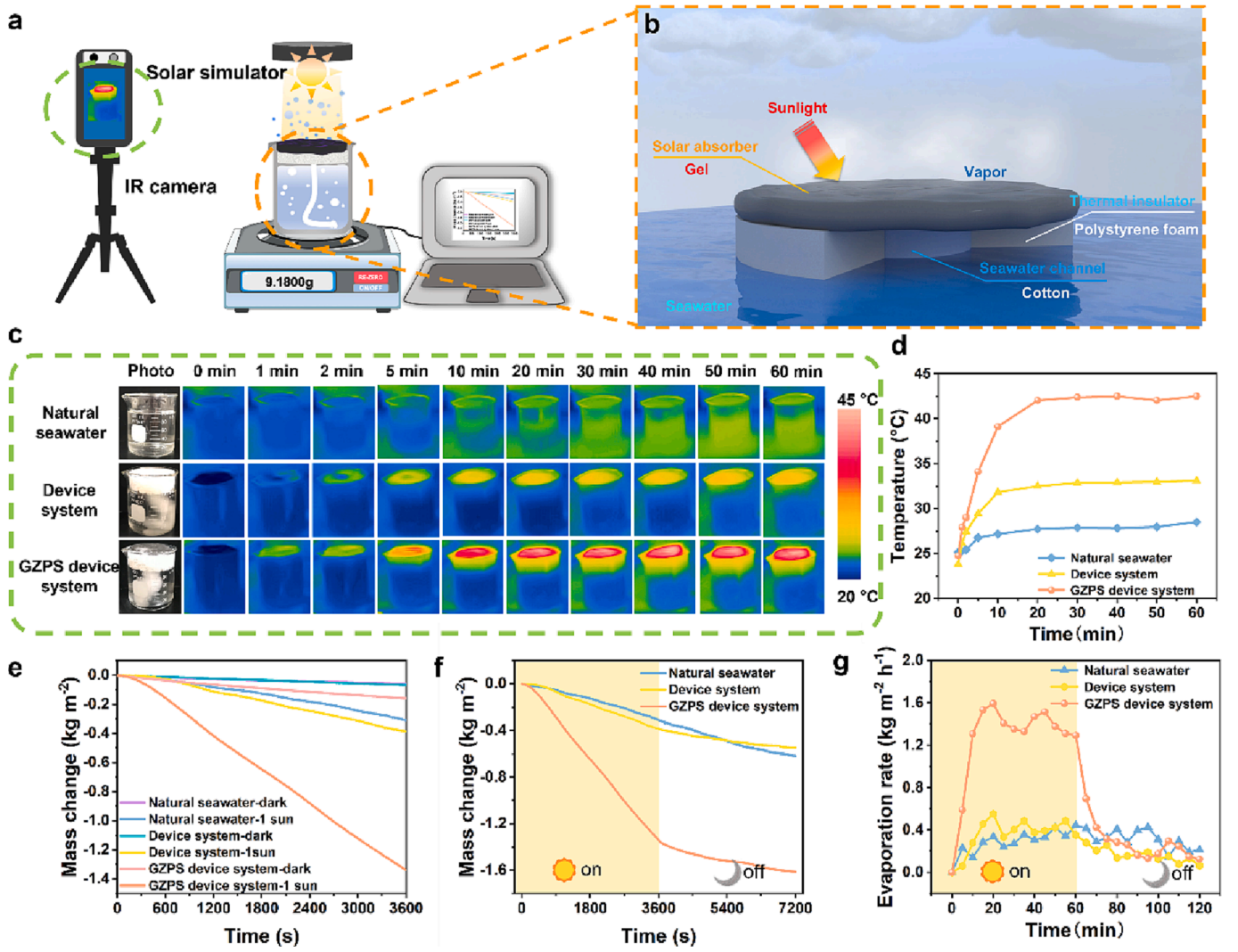

Fig. 6. (a) Schematic diagram of the solar-driven evaporation measurement system. (b) Specific appearance of the evaporator device system. (c) Thermal images of the natural seawater, the device system, and GZPS device system under 1 sun irradiation at various time points and (d) corresponding temperature changes. (e) Mass change curves depending on the time of the natural seawater, the device system, and GZPS device system under different conditions. (f) Mass change curves of the natural seawater, the device system, and GZPS device system under 1sun and in dark and the corresponding evaporation rate (g).

procedure A. in Supporting Information). It is worth noting that a complex polymeric network could cause reduce the evaporation enthalpy, so the corresponding efficiency was also calculated [11]. (See detailed calculation procedure B. and Fig. S15 in Supporting Information).

The excellent photothermal performance of GZPS device system benefits from its macro/micro/nano hierarchical structures that increase the optical path and reduce reflection through multiple scattering of incident light [68], as well as the excellent solar absorption and photothermal effect of ZIF-67 and graphene.

3.7. Practical application of GZPS evaporation device system

GZPS device system was tested for long-term usability and practical application effect. It has been carried out the cycle seawater evaporation experiment in solar light and darkness as well as long-term seawater evaporation experiment. To confirm the material's responsiveness to sunlight for photothermal conversion and its stability under different light conditions, a cyclic evaporation experiment was conducted. The experiment involved five cycles of turning on simulated solar radiation for one hour, followed by turning it off for one hour. The results show that the GZPS device system exhibited stable mass change trends during seawater evaporation, whether in the presence or absence of solar radiation. (Fig. 7a). It may be that the salt in the seawater is stored in the GZPS gel, which affects the subsequent long-term evaporation. According to the real-time efficiency, it can also be assumed that the highest efficiency can even reach over 1.89 kg m^{-2} h^{-1} at the beginning (Fig. 7b). In the subsequent continuous cycle evaporation experiment, even if the evaporation rate dropped to 1.03 kg m^{-2} h^{-1} when exposed to solar radiation, which still proves its durability and stability. The evaporated seawater was collected in a glass container in order to evaluate the effect of seawater desalination. As can be seen from Fig. 7c, there were obviously small water droplets of water vapor condensation in the glass container after evaporating for 3 min. As time went on, more and more water vapor condensed on the walls of the glassware (Video S1), and the photothermal effect is still significant when it evaporates even in the presence of the glassware. Ion concentration test was performed on the water collected after 12 h of continuous seawater evaporation, to verify the purification ability, including the four main metal ions of Na^+, Ca^{2+}, Mg^{2+}, K^+ and other metal ions including heavy metal ions (Mn^{2+}, Fe^{3+}, Co^{2+}, Ni^{2+}, Zn^{2+}, Pb^{2+}, Cd^{2+}, Cu^{2+}, Cr^{3+}). The concentrations of Na^+, Ca^{2+}, Mg^{2+} and K^+ sharply decreased to 6.61, 1.80, 5.61, and 2.95 mg L^{-1}, respectively, after solar purification (Fig. 7d). The concentration of other metal ions is also much lower than that of the

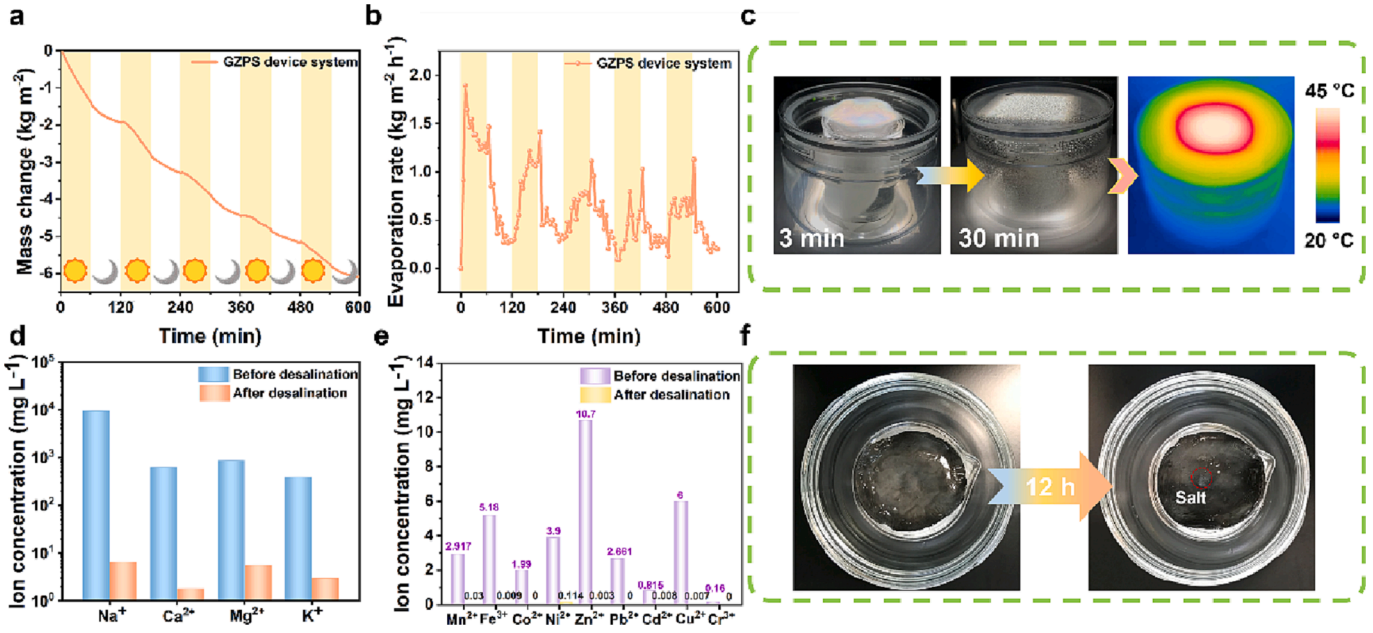

Fig. 7. (a) Mass change curve of the GZPS device system during the solar- driven seawater evaporation cyclic test, and the corresponding evaporation rate (b). (c) Photographs about the water droplets formation and the IR image during the evaporation. (d) The four main ion concentrations and other mental ion concentrations (e) in purified water and seawater. (f) The photos of GZPS device system before and after 12 h solar irradiation.

original seawater (Fig. 7e), demonstrating that photothermal evaporation has a strong removal effect on heavy metal ions.

The results show that the GZPS device system has excellent seawater purification and ion removal capabilities in solar-driven seawater evaporation. After a long term of evaporation, there is no obvious salt on the surface of GZPS gel. It is inferred that the hydrogel interior may contain salt, but this phenomenon does not strongly affect the surface appearance (Fig. 7f). This inference is verified by EDS distribution that a large amount of Na and Cl elements do appear in the hydrogel after long-term seawater evaporation experiment. Simultaneously, small amounts of other elements were also detected (Fig. S16), which proves its ability to adsorb ions.

According to the results, it can be inferred that the prepared GZPS hydrogel owns great potential in seawater desalination to produce clean water. The water production capacity of GZPS hydrogel, including water collection and evaporation, was compared with that of some recent research studies respectively, which demonstrated its excellent performance (Table S1 and S2).

4. Conclusions

In this study, a multifunctional macro/micro/nano hierarchical structure composite hydrogel (graphene/ZIF-67/PVA/SA) bioinspired by various organisms (*Selaginella lepidophylla*, honeycomb, pufferfish) has been successfully prepared after being assisted by facile water collection and evaporation enhancement device. It not only has outstanding performance in passive fog flow collection, accompanied by the collected water could be effectively released, but also has been successfully applied to solar-driven seawater desalination.

The synergistic effect of the hydrophilicity of the PVA/SA hydrogel matrix itself and the excellent solar absorption performance and ion adsorption capacity of the added functional nanomaterials graphene and ZIF-67 endow the composite hydrogel no matter in the dry or wet state produce clean water effectively. In the case of fog flow, the water uptake rate can reach 94.06% after 3 h, and the water release efficiency can reach up to 1.67 kg m^{-2} h^{-1} under the subsequent 1 sun irradiation. During natural seawater evaporation, with the integration of a rationally designed evaporation device system, the seawater evaporation rate even reached up to 1.89 kg m^{-2} h^{-1} with solar-heat conversion efficiency of 92.32%. This study facilitates scalable and modular applications for harvesting and purifying water from various sources assisted by clean renewable energy. Its special biomimetic strategy and structure as well as combination with facile and common props provide potential value for the application of functional materials, soft matter, gas adsorption and flexible power generation materials.

CRediT authorship contribution statement

Yi Zhang: Conceptualization, Methodology, Software, Formal analysis, Investigation, Writing – original draft. **Feifei Wang:** Methodology, Formal analysis. **Yongtao Yu:** Data curation, Investigation. **Jiajia Wu:** Methodology, Data curation. **Yingying Cai:** Methodology, Formal analysis. **Jian Shi:** Writing – review & editing, Supervision. **Hideaki Morikawa:** Project administration, Supervision. **Chunhong Zhu:** Writing – review & editing, Supervision.

Declaration of Competing Interest

The authors declare that they have no known competing financial interests or personal relationships that could have appeared to influence the work reported in this paper.

Data availability

Data will be made available on request.

Acknowledgments

This work was supported by JSPS KAKENHI (Grant number JP20H00288) and Japan-Egypt Research Cooperative Program between JSPS and STDF, grant number JPJSBP120206001.

Appendix A. Supplementary data

Supplementary data to this article can be found online at https://doi.org/10.1016/j.cej.2023.143330.

References

[1] S.H. Antwi, D. Getty, S. Linnane, A. Rolston, COVID-19 water sector responses in Europe: A scoping review of preliminary governmental interventions, Sci. Total Environ. 762 (2021), 143068, https://doi.org/10.1016/j.scitotenv.2020.143068.

[2] C.J. Vorosmarty, P. Green, J. Salisbury, R.B. Lammers, Global water resources: vulnerability from climate change and population growth, Science 289 (5477) (2000) 284–288, https://doi.org/10.1126/science.289.5477.284.

[3] D. Wang, Y. Chen, M. Jarin, X. Xie, Increasingly frequent extreme weather events urge the development of point-of-use water treatment systems, npj Clean Water 5 (1) (2022), https://doi.org/10.1038/s41545-022-00182-1.

[4] M.M. Mekonnen, A.Y. Hoekstra, Four billion people facing severe water scarcity, Sci. Adv. 2 (2) (2016) e1500323.

[5] Z. Zhang, H. Fu, Z. Li, J. Huang, Z. Xu, Y. Lai, X. Qian, S. Zhang, Hydrogel materials for sustainable water resources harvesting & treatment: Synthesis, mechanism and applications, Chem. Eng. J. 439 (2022), https://doi.org/10.1016/j.cej.2022.135756.

[6] G. Liu, T. Chen, J. Xu, G. Yao, J. Xie, Y. Cheng, Z. Miao, K. Wang, Salt-Rejecting Solar Interfacial Evaporation, Cell Reports Physical, Science 2 (1) (2021) 100310.

[7] H. Lu, W. Shi, Y. Guo, W. Guan, C. Lei, G. Yu, Materials Engineering for Atmospheric Water Harvesting: Progress and Perspectives, Adv. Mater. 34 (12) (2022) e2110079.

[8] J. Yang, J.B. van Lier, J. Li, J. Guo, F. Fang, Integrated anaerobic and algal bioreactors: A promising conceptual alternative approach for conventional sewage treatment, Bioresour. Technol. 343 (2022), 126115, https://doi.org/10.1016/j.biortech.2021.126115.

[9] N. Li, L. Luo, C. Guo, J. He, S. Wang, L. Yu, M. Wang, P. Murto, X. Xu, Shape-controlled fabrication of cost-effective, scalable and anti-biofouling hydrogel foams for solar-powered clean water production, Chem. Eng. J. 431 (2022), 134144, https://doi.org/10.1016/j.cej.2021.134144.

[10] L. Yang, N. Li, C. Guo, J. He, S. Wang, L. Qiao, F. Li, L. Yu, M. Wang, X. Xu, Marine biomass-derived composite aerogels for efficient and durable solar-driven interfacial evaporation and desalination, Chem. Eng. J. 417 (2021), 128051, https://doi.org/10.1016/j.cej.2020.128051.

[11] C. Li, B. Zhu, Z. Liu, J. Zhao, R. Meng, L. Zhang, Z. Chen, Polyelectrolyte-based photothermal hydrogel with low evaporation enthalpy for solar-driven salt-tolerant desalination, Chem. Eng. J. 431 (2022), 134224, https://doi.org/10.1016/j.cej.2021.134224.

[12] M.S. Irshad, N. Arshad, X. Wang, Nanoenabled Photothermal Materials for Clean Water Production, Glob Chall 5 (1) (2021) 2000055, https://doi.org/10.1002/gch2.202000055.

[13] P. Zhang, Q. Liao, H. Yao, Y. Huang, H. Cheng, L. Qu, Direct solar steam generation system for clean water production, Energy Storage Mater. 18 (2019) 429–446, https://doi.org/10.1016/j.ensm.2018.10.006.

[14] R. Li, Y. Shi, M. Wu, S. Hong, P. Wang, Improving atmospheric water production yield: Enabling multiple water harvesting cycles with nano sorbent, Nano Energy 67 (2020) 104255.

[15] G. Baggio, M. Qadir, V. Smakhtin, Freshwater availability status across countries for human and ecosystem needs, Sci. Total Environ. 792 (2021), 148230, https://doi.org/10.1016/j.scitotenv.2021.148230.

[16] X. Xu, N. Bizmark, K.S.S. Christie, S.S. Datta, Z.J. Ren, R.D. Priestley, Thermoresponsive Polymers for Water Treatment and Collection, Macromolecules 55 (6) (2022) 1894–1909, https://doi.org/10.1021/acs.macromol.1c01502.

[17] F. Li, N.a. Li, S. Wang, L. Qiao, L. Yu, P. Murto, X. Xu, Self-Repairing and Damage-Tolerant Hydrogels for Efficient Solar-Powered Water Purification and Desalination, Adv. Funct. Mater. 31 (40) (2021) 2104464.

[18] Y. Tu, R. Wang, Y. Zhang, J. Wang, Progress and Expectation of Atmospheric Water Harvesting, Joule 2 (8) (2018) 1452–1475, https://doi.org/10.1016/j.joule.2018.07.015.

[19] A. Lee, M.W. Moon, H. Lim, W.D. Kim, H.Y. Kim, Water harvest via dewing, Langmuir 28 (27) (2012) 10183–10191, https://doi.org/10.1021/la3013987.

[20] H. Park, I. Haechler, G. Schnoering, M.D. Ponte, T.M. Schutzius, D. Poulikakos, Enhanced Atmospheric Water Harvesting with Sunlight-Activated Sorption Ratcheting, ACS Appl. Mater. Interfaces 14 (1) (2022) 2237–2245, https://doi.org/10.1021/acsami.1c18852.

[21] B. Wang, X. Zhou, Z. Guo, W. Liu, Recent advances in atmosphere water harvesting: Design principle, materials, devices, and applications, Nano Today 40 (2021) 101283.

[22] H. Lu, W. Shi, J.H. Zhang, A.C. Chen, W. Guan, C. Lei, J.R. Greer, S.V. Boriskina, G. Yu, Tailoring the Desorption Behavior of Hygroscopic Gels for Atmospheric Water Harvesting in Arid Climates, Adv. Mater. 34 (37) (2022) e2205344.

[23] Y. Lin, K. Shao, S. Li, N. Li, S. Wang, X. Wu, C. Guo, L. Yu, P. Murto, X. Xu, Hygroscopic and Photothermal All-Polymer Foams for Efficient Atmospheric Water Harvesting, Passive Humidity Management, and Protective Packaging, ACS Appl. Mater. Interfaces 15 (7) (2023) 10084–10097, https://doi.org/10.1021/acsami.3c00302.

[24] J. He, N. Li, S. Wang, S. Li, C. Wang, L. Yu, P. Murto, X. Xu, Hygroscopic photothermal beads from marine polysaccharides: demonstration of efficient atmospheric water production, indoor humidity control and photovoltaic panel cooling, J. Mater. Chem. A 10 (15) (2022) 8556–8567, https://doi.org/10.1039/D2TA00594H.

[25] H. Zhu, Z. Guo, W. Liu, Biomimetic water-collecting materials inspired by nature, Chem. Commun. (Camb) 52 (20) (2016) 3863–3879, https://doi.org/10.1039/c5cc09867j.

[26] Y. Wang, S. Gao, W. Xu, Z. Wang, Nanogenerators with Superwetting Surfaces for Harvesting Water/Liquid Energy, Adv. Funct. Mater. 30 (26) (2020) 1908252.

[27] S. Wang, K. Liu, X. Yao, L. Jiang, Bioinspired surfaces with superwettability: new insight on theory, design, and applications, Chem. Rev. 115 (16) (2015) 8230–8293, https://doi.org/10.1021/cr400083y.

[28] Y. Zhang, N. Meng, A.A. Babar, X. Wang, J. Yu, B. Ding, Multi-bioinspired and Multistructural Integrated Patterned Nanofibrous Surface for Spontaneous and Efficient Fog Collection, Nano Lett. 21 (18) (2021) 7806–7814, https://doi.org/10.1021/acs.nanolett.1c02788.

[29] Y.i. Zhang, Y. Cai, J. Shi, H. Morikawa, C. Zhu, Multi-bioinspired hierarchical Janus membrane for fog harvesting and solar-driven seawater desalination, Desalination 540 (2022) 115975.

[30] Y. Zhang, N. Meng, A.A. Babar, X. Wang, J. Yu, B. Ding, Lizard-Skin-Inspired Nanofibrous Capillary Network Combined with a Slippery Surface for Efficient Fog Collection, ACS Appl. Mater. Interfaces 13 (30) (2021) 36587–36594, https://doi.org/10.1021/acsami.1c10067.

[31] Y. Zhang, C. Zhu, J. Shi, S. Yamanaka, H. Morikawa, Bioinspired Composite Materials used for Efficient Fog Harvesting with Structures that Consist of Fungi-Mycelia Networks, ACS Sustain. Chem. Eng. 10 (38) (2022) 12529–12539, https://doi.org/10.1021/acssuschemeng.2c01816.

[32] D. Curto, V. Franzitta, A. Guercio, A Review of the Water Desalination Technologies, Appl. Sci. 11 (2) (2021), https://doi.org/10.3390/app11020670.

[33] C. Zhu, A. Mochizuki, J. Shi, M. Ishimori, S. Koyama, H. Ishizawa, J. Yan, H. Morikawa, Photocatalytic self-cleaning coatings to remove oleic acid, an organic pollutant, from cotton fabrics, Cellul. 28 (12) (2021) 8139–8152, https://doi.org/10.1007/s10570-021-04004-4.

[34] C. Zhu, J. Shi, S. Xu, M. Ishimori, J. Sui, H. Morikawa, Design and characterization of self-cleaning cotton fabrics exploiting zinc oxide nanoparticle-triggered photocatalytic degradation, Cellul. 24 (6) (2017) 2657–2667, https://doi.org/10.1007/s10570-017-1289-7.

[35] Q. Zhao, J. Liu, Z. Wu, X. Xu, H. Ma, J. Hou, Q. Xu, R. Yang, K. Zhang, M. Zhang, H. Yang, W. Peng, X. Liu, C. Zhang, J. Xu, B. Lu, Robust PEDOT:PSS-based hydrogel for highly efficient interfacial solar water purification, Chem. Eng. J. 442 (2022), 136284, https://doi.org/10.1016/j.cej.2022.136284.

[36] Q. Zhao, Z. Wu, X. Xu, R. Yang, H. Ma, Q. Xu, K. Zhang, M. Zhang, J. Xu, B. Lu, Design of poly(3,4-ethylenedioxythiophene): polystyrene sulfonate-polyacrylamide dual network hydrogel for long-term stable, highly efficient solar steam generation, Sep. Purif. Technol. 300 (2022), 121889, https://doi.org/10.1016/j.seppur.2022.121889.

[37] Z. Lin, T. Wu, Y.F. Feng, J. Shi, B. Zhou, C. Zhu, Y. Wang, R. Liang, M. Mizuno, Poly(N-phenylglycine)/MoS(2) Nanohybrid with Synergistic Solar-Thermal Conversion for Efficient Water Purification and Thermoelectric Power Generation, ACS Appl. Mater. Interfaces 14 (1) (2022) 1034–1044, https://doi.org/10.1021/acsami.1c20393.

[38] Z. Lin, T. Wu, B. Jia, J. Shi, B.o. Zhou, C. Zhu, Y. Wang, R. Liang, M. Mizuno, Nature-inspired poly(N-phenylglycine)/wood solar evaporation system for high-efficiency desalination and water purification, Colloids Surf. A Physicochem. Eng. Asp. 637 (2022) 128272.

[39] L. Li, T. Hu, A. Li, J. Zhang, Electrically Conductive Carbon Aerogels with High Salt-Resistance for Efficient Solar-Driven Interfacial Evaporation, ACS Appl. Mater. Interfaces 12 (28) (2020) 32143–32153, https://doi.org/10.1021/acsami.0c06836.

[40] C. Ge, D. Xu, H. Du, Z. Chen, J. Chen, Z. Shen, W. Xu, Q. Zhang, J. Fang, Recent Advances in Fibrous Materials for Interfacial Solar Steam Generation, Adv. Fiber Mater. (2022), https://doi.org/10.1007/s42765-022-00228-6.

[41] J. Han, W. Xing, J. Yan, J. Wen, Y. Liu, Y. Wang, Z. Wu, L. Tang, J. Gao, Stretchable and Superhydrophilic Polyaniline/Halloysite Decorated Nanofiber Composite Evaporator for High Efficiency Seawater Desalination, Adv. Fiber Mater. 4 (5) (2022) 1233–1245, https://doi.org/10.1007/s42765-022-00172-5.

[42] Z. Liu, Z. Zhou, N. Wu, R. Zhang, B. Zhu, H. Jin, Y. Zhang, M. Zhu, Z. Chen, Hierarchical Photothermal Fabrics with Low Evaporation Enthalpy as Heliotropic Evaporators for Efficient, Continuous, Salt-Free Desalination, ACS Nano 15 (8) (2021) 13007–13018, https://doi.org/10.1021/acsnano.1c01900.

[43] D. Xu, Z. Zhu, J. Li, Recent Progress in Electrospun Nanofibers for the Membrane Distillation of Hypersaline Wastewaters, Adv. Fiber Mater. 4 (6) (2022) 1357–1374, https://doi.org/10.1007/s42765-022-00193-0.

[44] Z. Lin, T. Wu, J. Shi, B. Zhou, C. Zhu, Y. Wang, R. Liang, M. Mizuno, Poly(N-phenylglycine)-Based Bioinspired System for Stably and Efficiently Enhancing Solar Evaporation, ACS Sustain. Chem. Eng. 9 (1) (2020) 448–457, https://doi.org/10.1021/acssuschemeng.0c07608.

[45] Sedimentology and paleohydrology of late quaternary lake deposits in the Northern Namib Sand Sea, Namibia.

[46] F. Mvondo Owono, M.-J. Ntamak-Nida, O. Dauteuil, F. Guillocheau, B. Njom, Morphology and long-term landscape evolution of the South African plateau in South Namibia, Catena 142, Catena 142 (2016) 47–65.

[47] S.E. Evans, M.E. Dueker, J.R. Logan, K.C. Weathers, The biology of fog: results from coastal Maine and Namib Desert reveal common drivers of fog microbial composition, Sci. Total Environ. 647 (2019) 1547–1556, https://doi.org/10.1016/j.scitotenv.2018.08.045.

[48] A. Roth-Nebelsick, M. Ebner, T. Miranda, V. Gottschalk, D. Voigt, S. Gorb, T. Stegmaier, J. Sarsour, M. Linke, W. Konrad, Leaf surface structures enable the endemic Namib desert grass Stipagrostis sabulicola to irrigate itself with fog water, J. R. Soc. Interface 9 (73) (2012) 1965–1974, https://doi.org/10.1098/rsif.2011.0847.

[49] Z. Yu, H. Zhang, J. Huang, S. Li, S. Zhang, Y. Cheng, J. Mao, X. Dong, S. Gao, S. Wang, Z. Chen, Y. Jiang, Y. Lai, Namib desert beetle inspired special patterned fabric with programmable and gradient wettability for efficient fog harvesting,

J. Mater. Sci. Technol. 61 (2021) 85–92, https://doi.org/10.1016/j.jmst.2020.05.054.
[50] D. Gurera, B. Bhushan, Optimization of bioinspired conical surfaces for water collection from fog, J. Colloid Interface Sci. 551 (2019) 26–38, https://doi.org/10.1016/j.jcis.2019.05.015.
[51] N. Kyong Kim, D. Hee Kang, H. Eom, H., Wook Kang, Biomimetic fog harvesting surface by photo-induced micro-patterning of zinc-oxide silver hierarchical nanostructures, Appl. Surf. Sci. 470 (2019) 161–167, https://doi.org/10.1016/j.apsusc.2018.11.132.
[52] A. Yobi, B.W. Wone, W. Xu, D.C. Alexander, L. Guo, J.A. Ryals, M.J. Oliver, J. C. Cushman, Metabolomic profiling in Selaginella lepidophylla at various hydration states provides new insights into the mechanistic basis of desiccation tolerance, Mol. Plant 6 (2) (2013) 369–385, https://doi.org/10.1093/mp/sss155.
[53] A. Rafsanjani, V. Brule, T.L. Western, D. Pasini, Hydro-responsive curling of the resurrection plant Selaginella lepidophylla, Sci. Rep. 5 (2015) 8064, https://doi.org/10.1038/srep08064.
[54] Y. Zhang, L. Wu, A.A. Babar, X. Zhao, X. Wang, J. Yu, B. Ding, Honeycomb-Inspired Robust Hygroscopic Nanofibrous Cellular Networks, Small Methods 5 (11) (2021) e2101011.
[55] L. Heng, X. Meng, B. Wang, L. Jiang, Bioinspired design of honeycomb structure interfaces with controllable water adhesion, Langmuir 29 (30) (2013) 9491–9498, https://doi.org/10.1021/la401991n.
[56] J. Wang, C. Deng, G. Zhong, W. Ying, C. Li, S. Wang, Y. Liu, R. Wang, H. Zhang, High-yield and scalable water harvesting of honeycomb hygroscopic polymer driven by natural sunlight, Cell Reports Physical, Science 3 (7) (2022) 100954.
[57] P.C. Wainwright, R.G. Turingan, Evolution of Pufferfish Inflation Behavior, Evolution 51 (2) (1997) 506–518, https://doi.org/10.1111/j.1558-5646.1997.tb02438.x.
[58] X. Wang, S. Zhao, C. Li, X. Liu, J. Song, Neural basis of the stress response in a pufferfish, Takifugu obscurus, Integr. Zool. 10 (1) (2015) 133–140, https://doi.org/10.1111/1749-4877.12103.
[59] J. Fan, Z. Shi, M. Lian, H. Li, J. Yin, Mechanically strong graphene oxide/sodium alginate/polyacrylamide nanocomposite hydrogel with improved dye adsorption capacity, J. Mater. Chem. A 1 (25) (2013) 7433.
[60] W. Li, Y.Y. Liu, Y. Bai, J. Wang, H. Pang, Anchoring ZIF-67 particles on amidoximerized polyacrylonitrile fibers for radionuclide sequestration in wastewater and seawater, J. Hazard. Mater. 395 (2020), 122692, https://doi.org/10.1016/j.jhazmat.2020.122692.
[61] H.U. Rehman Shah, K. Ahmad, H.A. Naseem, S. Parveen, M. Ashfaq, A. Rauf, T. Aziz, Water stable graphene oxide metal-organic frameworks composite (ZIF-67@GO) for efficient removal of malachite green from water, Food Chem. Toxicol. 154 (2021) 112312.
[62] L. Li, Q. Li, Y. Feng, K. Chen, J. Zhang, Melamine/Silicone Hybrid Sponges with Controllable Microstructure and Wettability for Efficient Solar-Driven Interfacial Desalination, ACS Appl. Mater. Interfaces 14 (1) (2022) 2360–2368, https://doi.org/10.1021/acsami.1c20734.
[63] Fatma Tugce Senberber Dumanli, A.S. Kipcak, E.M. Derun, Microwave Dehydration of Borax: Characterization, Dehydration Kinetics, and Modelling, Glas. Phys. Chem. 48 (3) (2022) 210–218.
[64] X. Lou, Y.u. Huang, X. Yang, H. Zhu, L. Heng, F. Xia, External Stimuli Responsive Liquid-Infused Surfaces Switching between Slippery and Nonslippery States: Fabrications and Applications, Adv. Funct. Mater. 30 (10) (2020) 1901130.
[65] S. Yan, H. Song, Y. Li, J. Yang, X. Jia, S. Wang, X. Yang, Integrated reduced graphene oxide/polypyrrole hybrid aerogels for simultaneous photocatalytic decontamination and water evaporation, Appl. Catal. B 301 (2022) 120820.
[66] S. Bibi, E. Pervaiz, M. Ali, Synthesis and applications of metal oxide derivatives of ZIF-67: a mini-review, Chem. Pap. 75 (6) (2021) 2253–2275, https://doi.org/10.1007/s11696-020-01473-y.
[67] X. Zhou, F. Zhao, Y. Guo, B. Rosenberger, G. Yu, Architecting highly hydratable polymer networks to tune the water state for solar water purification, Sci. Adv. 5 (6) (2019) eaaw5484, https://doi.org/10.1126/sciadv.aaw5484.
[68] N. Li, L. Qiao, J. He, S. Wang, L. Yu, P. Murto, X. Li, X., Xu, Solar-Driven Interfacial Evaporation and Self-Powered Water Wave Detection Based on an All-Cellulose Monolithic Design, Adv. Funct. Mater. 31 (7) (2020), https://doi.org/10.1002/adfm.202008681.